



Article

Investigation of the Reversible Lithiation of an Oxide Free Aluminum Anode by a LiBH₄ Solid State Electrolyte

Jason A. Weeks ¹, Spencer C. Tinkey ¹, Patrick A. Ward ¹, Robert Lascola ², Ragaiy Zidan ^{1,*} and Joseph A. Teprovich Jr. ^{3,*}

¹ Secure Energy Manufacturing, Savannah River National Laboratory, Aiken, SC 29808, USA; Jason.Weeks@srnl.doe.gov (J.A.W.); Spencer.Tinkey@srnl.doe.gov (S.C.T.); patrick.ward@srs.gov (P.A.W.)

² Analytical Development, Savannah River National Laboratory, Aiken, SC 29808, USA; robert.lascola@srnl.doe.gov

³ Department of Chemistry and Biochemistry, College of Science and Math, California State University, Northridge, 18111 Nordhoff St., Northridge, CA 91334, USA

* Correspondence: ragaiy.zidan@srnl.doe.gov (R.Z.); joseph.teprovich@csun.edu (J.A.T.J.); Tel.: +01-818-677-4239 (J.A.T.J.)

Received: 19 September 2017; Accepted: 21 November 2017; Published: 23 November 2017

Abstract: In this study, we analyze and compare the physical and electrochemical properties of an all solid-state cell utilizing LiBH₄ as the electrolyte and aluminum as the active anode material. The system was characterized by galvanostatic lithiation/delithiation, cyclic voltammetry (CV), X-ray diffraction (XRD), energy dispersive X-ray spectroscopy (EDS), Raman spectroscopy, electrochemical impedance spectroscopy (EIS), and scanning electron microscopy (SEM). Constant current cycling demonstrated that the aluminum anode can be reversibly lithiated over multiple cycles utilizing a solid-state electrolyte. An initial capacity of 895 mAh/g was observed and is close to the theoretical capacity of aluminum. Cyclic voltammetry of the cell was consistent with the constant current cycling data and showed that the reversible lithiation/delithiation of aluminum occurs at 0.32 V and 0.38 V (vs. Li⁺/Li) respectively. XRD of the aluminum anode in the initial and lithiated state clearly showed the formation of a LiAl (1:1) alloy. SEM-EDS was utilized to examine the morphological changes that occur within the electrode during cycling. This work is the first example of reversible lithiation of aluminum in a solid-state cell and further emphasizes the robust nature of the LiBH₄ electrolyte. This demonstrates the possibility of utilizing other high capacity anode materials with a LiBH₄ based solid electrolyte in all-solid-state batteries.

Keywords: solid state electrolyte; LiBH₄; aluminum anode; lithium ion battery

1. Introduction

Global reliance on the need for portable power has led to the ubiquitous deployment of lithium ion batteries (LIB), prompting manufacturers to push the limits of current technologies through new cell design and packaging approaches. The recent fires and explosions of lithium ion batteries in consumer electronics and vehicles has served as a driving force for the investigation of solid state electrolytes in LIB. Solid electrolytes have the potential to serve as non-flammable alternatives to liquid electrolytes and allow for the use of metallic lithium as the anode and utilization of high capacity/voltage cathodes. Utilizing these high capacity materials as anodes and cathodes, in conjunction with a solid-state electrolyte in the next generation of LIB, will facilitate a significant increase in energy density, safety, and operation time.

Over the years, a number of solid state ionic conductors have been investigated such as lithium phosphorus oxynitride (LiPON) [1], Li₇La₃Zr₂O₁₂ (LLZO) [2], and lithium thiophosphates

(LPS) [3]. Recent interest in utilizing LiBH_4 as a solid-state electrolyte was established through the work of Orimo [4], who demonstrated that the ionic conductivity of lithium can be greater than 1 mS/cm at temperatures above the orthorhombic to hexagonal phase transition that occurs at 380 K [5]. This work has been expanded to achieve high conductivity in LiBH_4 based solid electrolytes through the addition of Li halide salts [6–8], nanoconfinement [9–12], nanoionic destabilization [13,14], ion substitution [15–21], and eutectic formation [22].

It has also been demonstrated that LiBH_4 can be utilized as a solid-state electrolyte in a $\text{Li}/\text{LiBH}_4/\text{LiCoO}_2$ configuration [23]. This work utilized a PLD thin film of LiCoO_2 that was coated with a Li_3PO_4 protecting layer to mitigate a chemical reaction from occurring at the $\text{LiBH}_4/\text{Li}_{1-x}\text{CoO}_2$ interface. Since this work, researchers have also expanded the utilization of a LiBH_4 electrolyte with high capacity electrode materials including sulfur [24–26], silicon [14], TiS_2 [27,28] and $\text{MgH}_2/\text{TiH}_2$ [26]. Aluminum anodes have previously been investigated as a potential high capacity anode in lithium ion cells due to its low cost, low lithiation/delithiation potential (0.32 V and 0.38 V respectively), high electrical conductivity, and high theoretical capacity (993 mAh/g) in traditional liquid based electrolytes [29]. However, to the best of our knowledge, no one has demonstrated the reversible lithiation of aluminum in the solid state or with a LiBH_4 electrolyte.

An aluminum composite was chosen as the anode for the cell, because aluminum anodes have much higher theoretical capacities than conventional carbon-anodes (372 mAh/g) [30]. Carbon does have a lower plateau potential of lithiation (<0.09 V vs. Li^+/Li) [30] than aluminum (~0.3 V vs. Li^+/Li) [31]. However, this low plateau potential of the carbon anode could be problematic because it can facilitate lithium plating and subsequent dendrite growth on the electrode surface leading to shorting and cell failure. The most commonly studied metal oxide based anode that is also used in commercial lithium ion batteries is lithium titanate (LTO). The main problem with LTO is that it has a much lower capacity (~170 mAh/g) [32] than graphite. However, its plateau potential is much higher (~1.5 V vs. Li^+/Li) [32] and would eliminate the possibility of lithium plating and dendrite formation. Although LTO can be paired with a high voltage cathode (≥ 4.8 V), its operating voltage in a full cell is typically less than 2.4 V [32]. The aluminum anode would have a much higher operating voltage (>3.5 V) [29] in a full cell set-up than LTO when coupled with a high voltage cathode. The novel electrochemical properties of an aluminum anode make it a unique anode candidate in the solid-state.

The increased energy demand from batteries has led to the investigation of novel high capacity anode/cathode materials as well as solid state electrolytes. This paper address two of the three research needs for the next generation of lithium ion batteries through the investigation of the solid-state electrolyte LiBH_4 paired with a high capacity anode candidate, aluminum. The goal of the work is to further expand this field to include new high capacity anodes that can be paired and successfully cycled with LiBH_4 or other composite metal hydride based solid state electrolytes.

2. Results and Discussion

Aluminum has a native oxide layer (~4 nm thick) on the surface of the material which must be traversed in order to achieve reversible lithiation/delithiation. Others have investigated the use of thermal evaporation to produce thin films [29], nanopillar aluminum arrays [33,34], or various particle sizes [35]. To avoid this native oxide layer and provide a high surface area aluminum to interact with Li^+ , we utilized decomposed alane (AlH_3) as the source of aluminum [36,37]. To obtain the aluminum used for this work, a sample of alane was dehydrogenated under inert conditions to produce high surface area aluminum nanoparticles that are free of the native oxide layer on the surface (Figure 1).

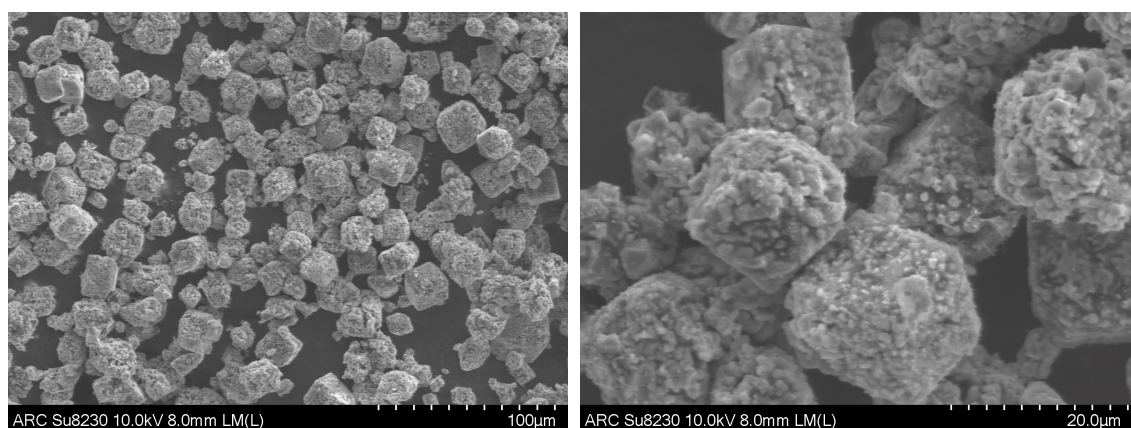


Figure 1. SEM of the aluminum obtained from the dehydrogenation of alane and utilized to prepare the composite anode material.

To determine if aluminum can be lithiated in the solid state, a composite electrode was prepared with aluminum as the active material (Al), LiBH_4 to facilitate Li^+ ion transport through the composite, carbon black (CB) to provide electrical conductivity, and polyvinylidene fluoride (PVDF) as a binder. The composite anode was pressed into a nickel foam (~2–4 mg) and then pelletized with LiBH_4 (~90 mg). Li foil was then attached to the opposite side and the pellet was sandwiched between two nickel disks and compressed with a spring inside of a 1/2 in. Swagelok union with two electrode posts (Figure 2). To enhance the ionic conductivity of LiBH_4 and allow for the even distribution of the solid electrolyte throughout the aluminum composite anode, it was Spex milled as previously described [38,39].

The cycling of the aluminum composite anode in the solid state with LiBH_4 as the solid-state electrolyte (Figure 3) is consistent with our previous study of aluminum (derived from AlH_3) based anodes in a liquid electrolyte (1.0 M LiPF_6 in EC/DMC) [40]. During the first cycle, a capacity of 895 mAh/g is achieved which is close to the theoretical capacity of a (1:1) LiAl alloy (993 mAh/g).

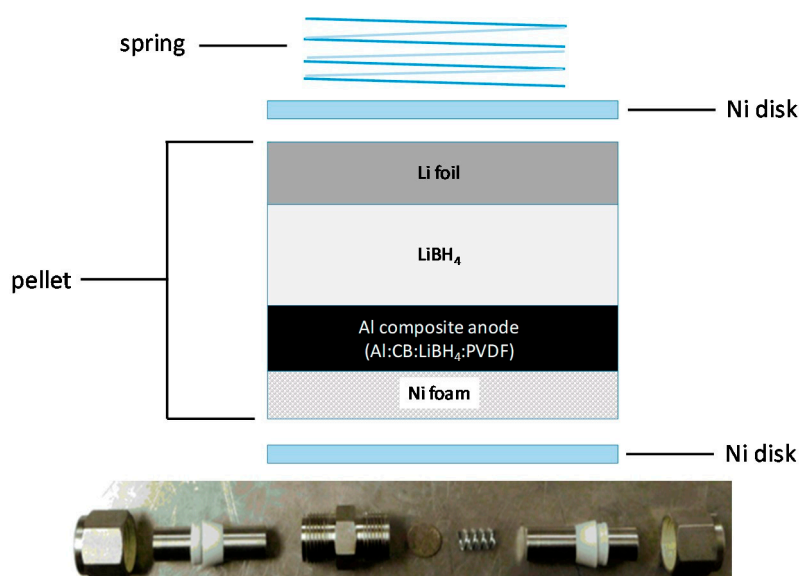


Figure 2. (Top) Schematic of the pellet inserted inside of the (bottom) Swagelok cell utilized for the electrochemical characterization.

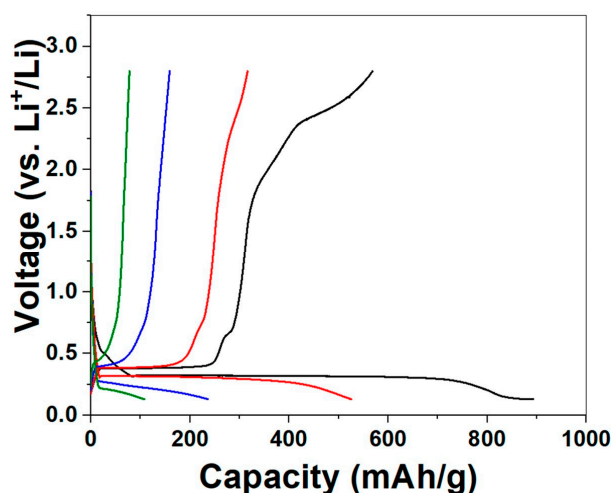


Figure 3. Lithiation/delithiation cycles of the Li/LiBH₄/Al composite cell. Cycling was performed at 0.1 C between 0.13 and 2.8 V (vs. Li⁺/Li) at 135 °C. Cycle number: Black—1st, Red—2nd, Blue—5th, and Green—10th.

Subsequent cycling of the material results in a loss in capacity. This behavior is common to aluminum based anode materials and is likely attributed to the low lithium diffusion coefficient in LiAl which is $6 \times 10^{-12} \text{ cm}^{-2} \cdot \text{s}^{-1}$ at 298 K [29]. This is likely the primary cause of low reversibility in the system due to the lithium being trapped within the LiAl alloy formed during the 1st and subsequent lithiation cycles. This same type of behavior has also been observed in the solution state and is due to lithium entrapment during the LiAl alloy formation [41]. In the same study, authors also report a phase transformation from α -LiAl to β -LiAl which occurs via a solid solution mediated crystallization to form the β -LiAl phase when an Al foil anode is utilized. Additional cycling studies were also performed to understand how the cycling rate effects the capacity retention (Figure 4). Cycling rates of 0.1 C, 0.5 C, and 1.0 C, based on the amount of aluminum within the anode, were also evaluated for the system. This indicates that the LiBH₄ can potentially support high charge/discharge rates.

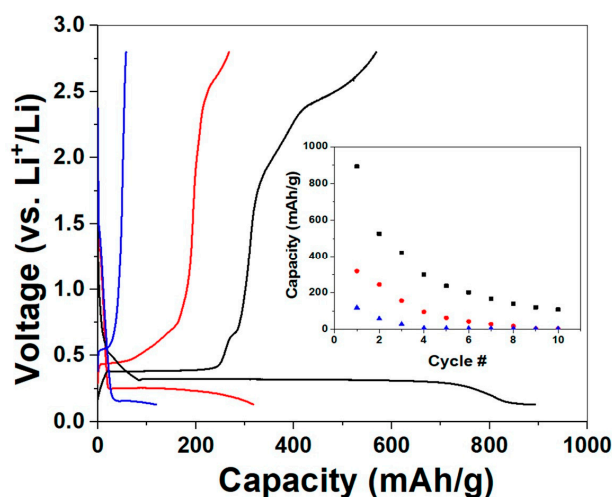


Figure 4. Effect of cycling rate on the first cycle capacity of the Li/LiBH₄/Al composite cell at 135 °C. Inset shows the capacity as a function of cycling rate over the first 10 cycles. Black—0.1 C, Red—0.5 C, and Blue—1.0 C.

CV was performed on the Li/LiBH₄/Al composite cell at 135 °C from 2.8 V to 0.13 V vs. Li⁺/Li (Figure 5). The CV was consistent with the galvanostatic charging/discharging experiments over the

potential window. The CV clearly shows the onset of lithiation at 0.32 V while the delithiation onset occurs at 0.38 V. With each subsequent cycle, the area of the oxidation and reduction peaks in the CV gradually decreases as observed in the cycling experiments.

To understand how the morphology of the Al composite electrode changed with cycling, SEM analysis was performed (Figure 6). SEM clearly showed the presence of spherical shaped particles (20–40 μm in diameter) and a relatively smooth surface of the electrode in the as prepared state. However, after the lithiation cycle of the aluminum, these spherical particles are no longer present. Additionally, the surface increases in roughness and the formation of voids within the electrode are clearly present. The formation of a rough surface and the creation of voids within the electrode could be due to the lattice expansion that occurs during the lithiation of aluminum to form the LiAl alloy. Going from metallic aluminum to the LiAl alloy results in a 97% expansion in the lattice [42]. However, this is significantly less than the lattice expansion during the lithiation of Si to $\text{Li}_{22}\text{Si}_5$ and Sn to $\text{Li}_{22}\text{Sn}_5$ which are 323% and 300% [43] respectively. The expansion of these 3 alloys are all significantly more than the graphite electrode currently utilized in commercial LIB, which expands only 9% upon lithiation [44].

Next, SEM-EDS was utilized to ascertain the identity of the spherical particles and obtain chemical information about the surface. Figure 7 shows the elemental distribution of B, Al, F, O, and C on the surface of the aluminum composite anode in the initial state. By looking at the boron distribution it is more concentrated around the spherical particles indicating that they are composed of LiBH_4 . The aluminum particles are also clearly distinguishable. The distribution mapping of carbon from the CB and PVDF and the fluorine from PVDF are nearly identical. Oxygen is also present in the sample but it has a very low concentration where the aluminum particles are present and is consistent with our hypothesis that the aluminum is relatively free of an oxide layer.

SEM-EDS was then taken of the aluminum composite electrode after the first lithiation (Figure 8). The distribution of boron throughout the electrode is significantly affected by this process because it is now randomly distributed through the sample and not concentrated in a certain location/particle. This is also consistent with the disappearance of the spherical shapes that were identified as LiBH_4 in Figure 7. This unique morphological change has not been previously reported for a solid-state cell utilizing pure LiBH_4 as a solid electrolyte. This was unexpected because LiBH_4 does not melt until $>275\text{ }^\circ\text{C}$. However, the operation temperature of the cell is above the orthorhombic to hexagonal phase transition that occurs at temperatures $>115\text{ }^\circ\text{C}$, and could be responsible for the change in morphology. Further investigation of this morphological change and its possible impact on electrochemical systems is needed.

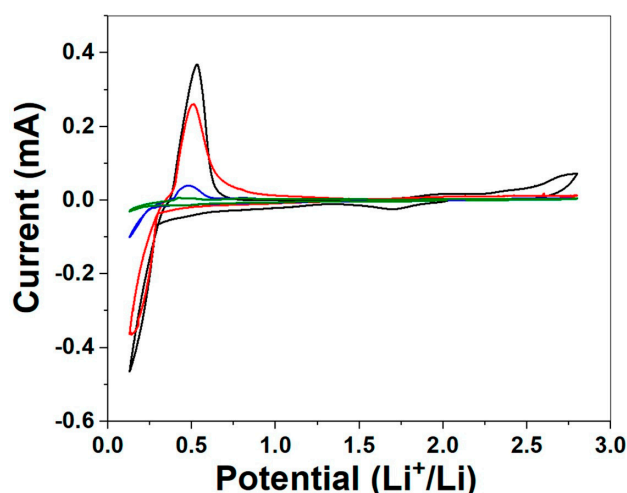


Figure 5. Cyclic voltammogram of the Li/LiBH₄/Al composite cell at 135 °C. Cycle number: Black—1st, Red—2nd, Blue—5th, and Green—10th.

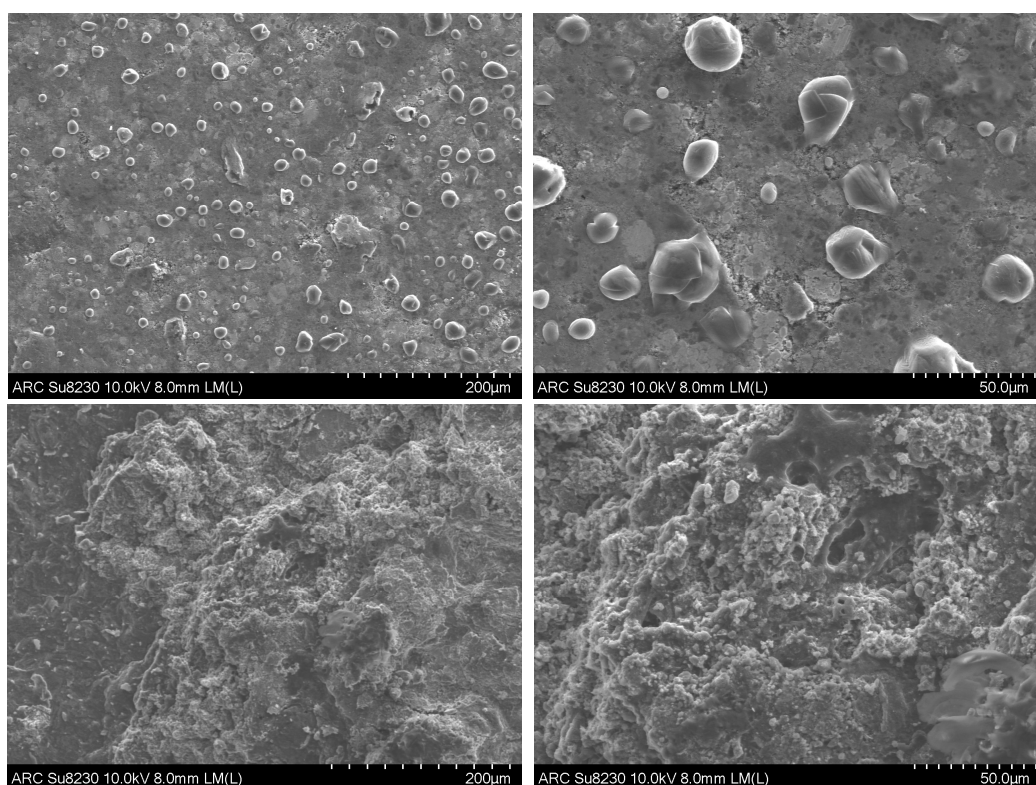


Figure 6. (Top, left and right) Wide field view and zoomed in view of the Al composite anode side of the pellet in the initial state. (Bottom, left and right) Wide field view and zoomed in view of the Al composite anode side of the pellet after the first lithiation.

The aluminum signal is still present in the sample; however, the edges of the aluminum particles are less sharp and not as defined which could be due to pulverization during the lithiation. The oxygen content of the sample is significantly increased in the sample; however, this could have occurred during the cycling of the sample in the Swagelok cell or during the brief exposure of the sample to air when it is introduced into the SEM for analysis.

XRD was utilized to confirm that the electrochemical plateaus observed during the galvanostatic charge/discharge cycles were attributed to the formation of a LiAl alloy (Figure 9). To do this a pellet was assembled as described in Figure 2, however, the Ni foam was excluded from the process so that diffraction pattern wouldn't be dominated by the high Z nickel. In the initial state (before lithiation) the presence of aluminum is confirmed in the XRD (denoted as *). After the first lithiation, the formation of the LiAl alloy (denoted as #) is then observed with the formation of 4 well defined and resolved peaks. There are still pure aluminum peaks present in the diffraction pattern and is attributed to the fact that the Li^+ must diffuse all of the way through the electrolyte and then the full thickness of electrode to achieve lithiation at the bottom of the pellet. It may be possible to demonstrate full conversion of aluminum to the LiAl alloy, but it would require a much slower lithiation rate and reduced thickness of the composite electrode. However, the purpose of this experiment was to spectroscopically verify the formation of the LiAl alloy via lithium migration through the LiBH_4 electrolyte. The unlabeled peaks in the spectrum are from the LiBH_4 used in the composite electrode and as the solid-state electrolyte.

To further characterize the interface between the electrodes and electrolyte electrochemical impedance spectroscopy (EIS) and Raman spectroscopy was performed (Figure 10). The EIS spectra for the cell ($\text{Li}/\text{LiBH}_4/\text{Al}$) at room temperature before cycling is shown in the inset. The Nyquist plot for this sample shows a very large resistance for the electrolyte and the charge transfer process occurring at the interface of the electrolyte/electrodes. Upon heating to $135\text{ }^\circ\text{C}$, there is a significant

reduction in the resistance for the electrolyte and the charge transfer at the interface as expected before cycling. After the first cycle, there is a reduction in the resistance of the electrolyte. This is likely due to disappearance of the spherical LiBH_4 particles (observed in the SEM-EDS) resulting in better Li ion diffusion at the interface. After the 10th cycle, the resistance of the electrolyte and charge transfer increases and is likely due to the large volume expansion/contraction of the Al active material during the lithiation/delithiation process. This likely results in small gaps at the electrode-electrolyte interface which effectively closes the lithium ion transport into and out of the Al.

Raman spectroscopy was carried out on the anode side of the electrolyte pellet in the as prepared sample and after 5 cycles at room temperature. For these experiments, PDVF and CB were removed from the anode for clarity and to obtain suitable spectra due to the absorbance of scattered light from the black carbon material. The B–H vibration modes [45], shown in Figure 10, demonstrate no significant change in frequency due to the formation of additional Li–B–H species, such as $\text{Li}_2\text{B}_{12}\text{H}_{12}$, and are consistent with orthorhombic LiBH_4 . This is expected since the hexagonal phase is only stabilized at high temperatures or with the incorporation of suitable additives [7].

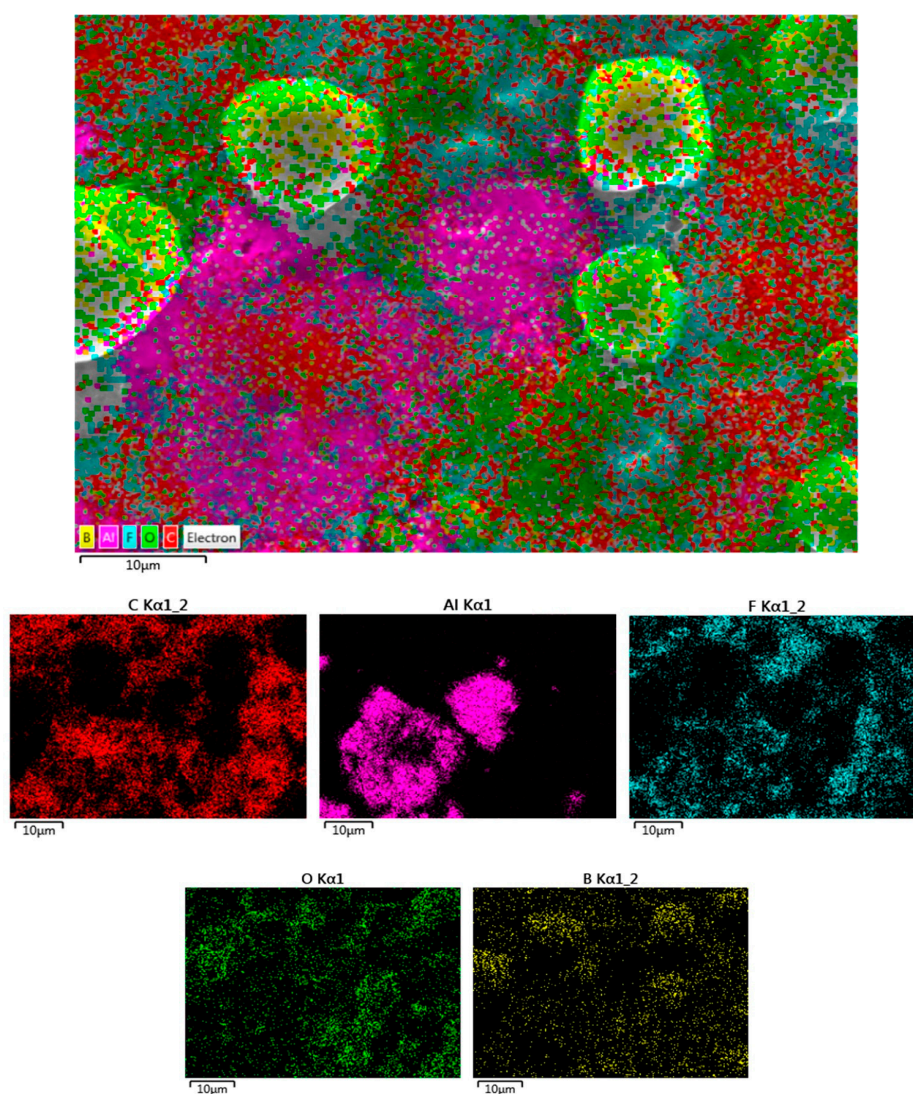


Figure 7. SEM-EDS of the aluminum composite anode in the initial state. The top image is the composite map of carbon, aluminum, fluorine, oxygen, and boron elemental distribution. The bottom images are the individual atomic distributions of the elements.

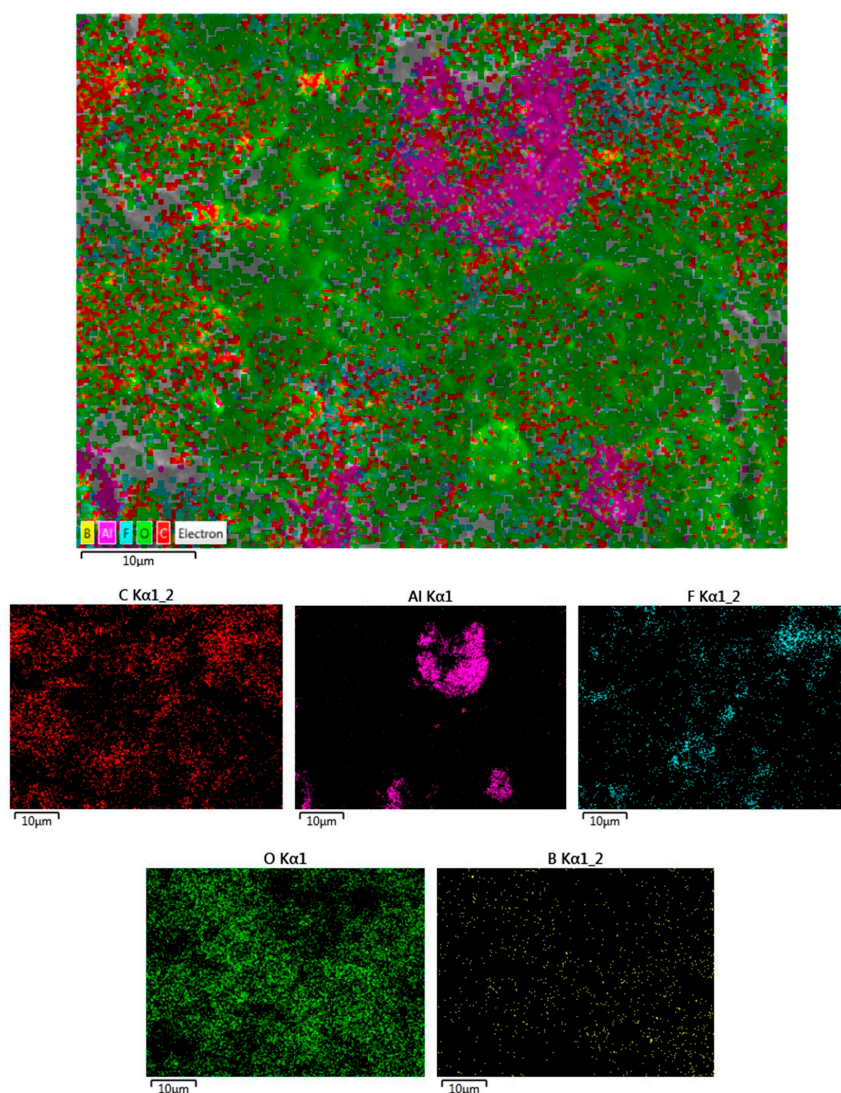


Figure 8. SEM-EDS of the aluminum composite anode after the first lithiation. The top image is the composite map of carbon, aluminum, fluorine, oxygen, and boron elemental distribution. The bottom images are the individual atomic distributions of the elements.

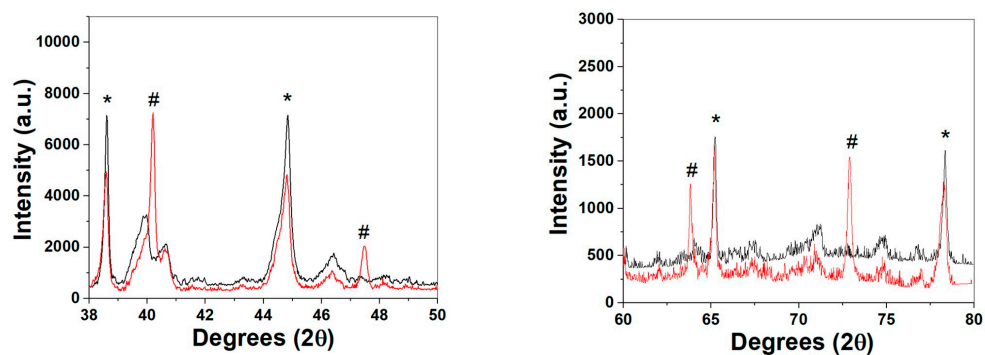


Figure 9. XRD of the aluminum anode composite before (black) and after the 1st lithiation cycle (red). The left and the right panels show the low 2θ and high 2θ respectively. Aluminum (*, pdf 00-0040787) and LiAl alloy (#, pdf 01-072-3428).

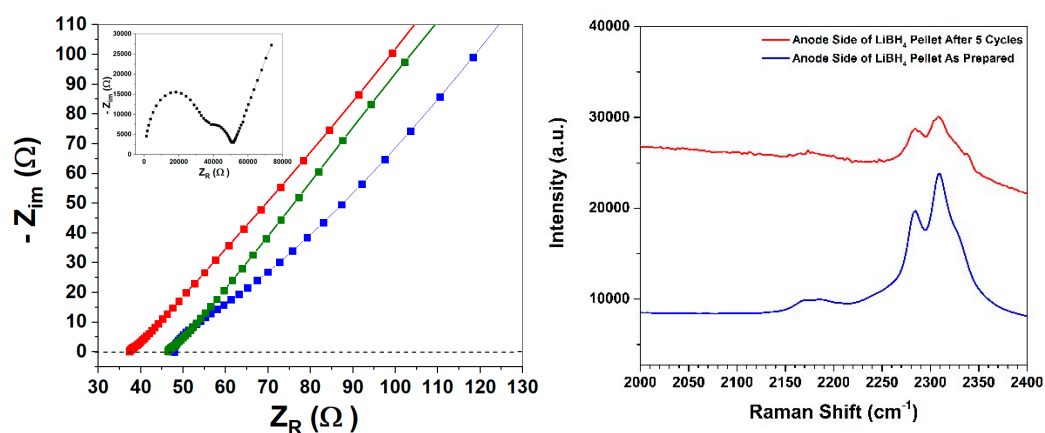


Figure 10. (Left) Electrochemical impedance spectroscopy (EIS) of the Li/LiBH₄/Al cell. The inset (black) shows the cell at room temperature. The other 3 EIS traces are for the cell at 135 °C before cycling (blue), after the 1st cycle (red), and after the 10th cycle (green). (Right) Raman spectra of the B–H stretching modes of LiBH₄ in the as prepared electrolyte pellet from the anode side (blue) and after cycling five times (red).

3. Materials and Methods

3.1. Materials

Chemicals were provided by the supplier and are listed by supplier as follows. Sigma Aldrich (St. Louis, MO, USA): LiBH₄ and lithium foil; MTI corp. (Richmond, CA, USA): TIMCAL graphite carbon super P (CB) and polyvinylidene fluoride (PVdF). Aluminum (Al) utilized as the anode material was obtained from the dehydrogenation of AlH₃ (ATK) at 220 °C under a constant argon flow on a Schlenk line for 2 h.

3.2. Electrolyte and Anode Preparation

LiBH₄ was ball milled for a total of thirty minutes with a 30:1 ball to powder ratio utilizing a SPEX ball mill. After ball milling, the LiBH₄ material was ground up with the use of a mortar and pestle. The aluminum composite was prepared with equal parts of activated aluminum; LiBH₄; PVdF; and CB (mass ratio of 10:6:3:3 respectively). This mixture was then homogenized with the use of a mortar and pestle. The pellets were assembled by first obtaining a flattened nickel foam current collector and manually pressing the aluminum composite anode material (2.0–3.0 mg) into it. The foam was then placed at the bottom of a die 10 mm die set (International Crystal Laboratories) with the aluminum anode composite facing up. Next, approximately ~90 mg of LiBH₄ was added on top of the nickel foam/anode composite. The die set was then fully assembled and pressed in a hydraulic press at 2 tons of pressure. After the pellet was pressed, it was removed from the die set with the nickel foam/anode composite attached to one side of the LiBH₄ pellet.

3.3. Cell Assembly and Electrochemical Characterization

Electrochemical measurements were performed using a Swagelok cell. The cells contained two polished nickel disk current collectors. The nickel foam/anode composite/LiBH₄/Li foil pellet was placed between two solid nickel disks to maintain sufficient electrical connectivity and provide uniform pressure on the pellet while in the cell under the pressure of a spring. The inside of the Swagelok cell was lined with a Mylar film and Teflon ferrules that were used to prevent shorting. The measurements were taken on a Bio-Logic VMP3 multichannel potentiostat (Bio-Logic Ltd., Grenoble, France). In order to increase the conductivity of the LiBH₄ electrolyte and reduce the contact resistance at the electrode/electrolyte interfaces, the cells were electrochemically evaluated at

135 °C. The heating process was conducted with the use of heating tape submerged in a sand bath. The temperature was monitored with the use of a K-type thermocouple positioned against the wall of the Swagelok cell. The cells were then cycled at various rates (0.1 C, 0.5 C, and 1.0 C) based on the amount of aluminum in the composite anode, for conducting galvanostatic charging/discharging of the cells. Cyclic voltammograms were collected at a cycling rate of 0.100 mV/s with a voltage window of 0.13 V to 2.80 V. The EIS was measured in a frequency range of 1 MHz to 100 Hz at ± 20 mV amplitude.

3.4. Ex-Situ XRD, SEM-EDS, and Raman Characterization

XRD was utilized to confirm the formation of the LiAl alloy after the first lithiation cycle. For this set-up, the anode composite was pressed into the LiBH₄ pellet without the use of the nickel foam current collector. This was done to eliminate the large signal from the nickel foam current collector during the XRD data collection. This allowed for the aluminum and the LiAl alloy to be readily detectable during the analysis. XRD was performed using a PANalytical X'pert Pro (PANalytical Ltd., Almelo, The Netherlands) with Cu K α radiation, and the samples were protected with a Kapton film to minimize oxidation of the sample.

SEM was used to analyze the change in surface morphology that occurred as a result of lithiating the active material. This process was done with the use of a Hitachi Ultra-High Resolution Scanning Electron Microscope SU8230 series (Hitachi, Ltd., Tokyo, Japan) with an X-Max^{II} Silicon Drift Detector attachment. Further atomic composition studies (EDS) were performed and the data from the analysis was interpreted using Aztec software.

Raman spectra were obtained with 15 mW 532 nm excitation using a 5 mm focal length optical fiber probe focused onto the pellet surface. Spectra were recorded at ~ 5 cm⁻¹ resolution using a Holospec transmission grating spectrometer (Andor Technology Ltd., Belfast, UK) with CCD detection.

4. Conclusions

In this study, we demonstrated the reversible electrochemical lithiation of a composite aluminum anode facilitated by a LiBH₄ solid state electrolyte. It was also demonstrated that the LiBH₄ solid state electrolyte can facilitate the reversible lithiation of aluminum at charge/discharge rates up to 1.0 C. Also, this study showed that metal hydrides (such as AlH₃) can serve as the source of oxide free metals for battery applications. XRD confirmed the formation of a LiAl alloy after the first lithiation cycle. SEM analysis identified unique morphological changes that occur within the electrode during the cycling of the material. It is likely that similar changes are also occurring in other cells that utilize a LiBH₄ based material as the solid electrolyte. This type of morphological change should also be considered along with other expansion/contraction processes in the high capacity anode materials in future studies. A better understanding of this mechanism will be needed for the further development of LiBH₄ based electrolytes. Although the cycle stability of the aluminum composite anode is poor, recent work has also investigated an Al/TiO₂ yolk-shell nano-architecture (ATO) that facilitates reversible lithiation/delithiation of aluminum for 500 cycles with excellent capacity retention [46]. Our future work will focus on this type of architecture in combination with the LiBH₄ based electrolyte as well as the closo-borane solid state electrolytes.

Acknowledgments: Work at SRNL was supported by the U.S. Department of Energy, Office of Science, Basic Energy Sciences, Materials Sciences and Engineering Division. Joseph A. Teprovich would like to thank the California State University—Northridge, College of Science & Mathematics start-up funding for support.

Author Contributions: Joseph A. Teprovich Jr. and Ragaiy Zidan conceived and designed the experimental approach. Jason A. Weeks, Spencer C. Tinkey and Patrick A. Ward performed the electrochemical and spectroscopic analysis of the materials. Robert Lascola performed the Raman analysis of the materials and interface. All of the authors wrote, commented, and contributed to the manuscript.

Conflicts of Interest: The authors declare no conflict of interest.

References

1. Yu, X.; Bates, J.B.; Jellison, G.E.; Hart, F.X. A Stable Thin-Film Lithium Electrolyte: Lithium Phosphorus Oxynitride. *J. Electrochem. Soc.* **1997**, *144*, 524–532. [[CrossRef](#)]
2. Murugan, R.; Thangadurai, V.; Weppner, W. Fast Lithium Ion Conduction in Garnet-Type $\text{Li}_7\text{La}_3\text{Zr}_2\text{O}_{12}$. *Angew. Chem. Int. Ed.* **2007**, *46*, 7778–7781. [[CrossRef](#)] [[PubMed](#)]
3. Liu, Z.; Fu, W.; Payzant, E.A.; Yu, X.; Wu, Z.; Dudney, N.J.; Kiggans, J.; Hong, K.; Rondinone, A.J.; Liang, C. Anomalous High Ionic Conductivity of Nanoporous β Li_3PS_4 . *J. Am. Chem. Soc.* **2013**, *135*, 975–978. [[CrossRef](#)] [[PubMed](#)]
4. Matsuo, M.; Nakamori, Y.; Orimo, S.; Maekawa, H.; Takamura, H. Lithium superionic conduction in lithium borohydride accompanied by structural transition. *Appl. Phys. Lett.* **2007**, *91*, 224103. [[CrossRef](#)]
5. Gorbunov, V.E.; Gavrichev, K.S.; Zalukaev, V.L.; Sharpataya, G.A.; Bakum, S.I. Heat capacity and phase transition of lithium borohydride. *Zhurnal Neorganicheskoy Khimii* **1984**, *29*, 2333–2337.
6. Maekawa, H.; Matsuo, M.; Takamura, H.; Ando, M.; Noda, Y.; Karahashi, T.; Orimo, S. Halide-Stabilized LiBH_4 , a Room-Temperature Lithium Fast-Ion Conductor. *J. Am. Chem. Soc.* **2009**, *131*, 894–895. [[CrossRef](#)] [[PubMed](#)]
7. Matsuo, M.; Takamura, H.; Maekawa, H.; Li, H.; Orimo, S. Stabilization of lithium superionic conduction phase and enhancement of conductivity of LiBH_4 by LiCl addition. *Appl. Phys. Lett.* **2009**, *94*, 084103. [[CrossRef](#)]
8. Skripov, A.V.; Soloninin, A.V.; Rude, L.H.; Jensen, T.R.; Filinchuk, Y. Nuclear Magnetic Resonance Studies of Reorientational Motion and Li Diffusion in LiBH_4 -LiI Solid Solutions. *J. Phys. Chem. C* **2012**, *116*, 26177–26184. [[CrossRef](#)]
9. Choi, Y.S.; Lee, Y.; Oh, K.H.; Cho, Y.W. Interface-enhanced Li ion conduction in a LiBH_4 - SiO_2 solid electrolyte. *Phys. Chem. Chem. Phys.* **2016**, *18*, 22540–22547. [[CrossRef](#)] [[PubMed](#)]
10. Shane, D.T.; Corey, R.L.; McIntosh, C.; Rayhel, L.H.; Bowman, R.C., Jr.; Vajo, J.J.; Gross, A.F.; Conradi, M.S. LiBH_4 in Carbon Aerogel Nanoscaffolds: An NMR Study of Atomic Motions. *J. Phys. Chem. C* **2010**, *114*, 4008–4014. [[CrossRef](#)]
11. Blanchard, D.; Nale, A.; Sveinbjornsson, D.; Eggenhuisen, T.M.; Verkuijlen, M.H.; Vegge, T.; Kentgens, A.P.; de Jongh, P.E. Nanoconfined LiBH_4 as a fast lithium ion conductor. *Adv. Funct. Mater.* **2015**, *25*, 184–192. [[CrossRef](#)]
12. Das, S.; Ngene, P.; Norby, P.; Vegge, T.; de Jongh, P.E.; Blanchard, D. All-Solid-State Lithium-Sulfur Battery Based on a Nanoconfined LiBH_4 Electrolyte. *J. Electrochem. Soc.* **2016**, *163*, A2029–A2034. [[CrossRef](#)]
13. Shane, D.T.; Corey, R.L.; Rayhel, L.H.; Wellons, M.; Teprovich, J.A., Jr.; Zidan, R.; Hwang, S.; Bowman, R.C., Jr.; Conradi, M.S. NMR Study of LiBH_4 with C_{60} . *J. Phys. Chem. C* **2010**, *114*, 19862–19866. [[CrossRef](#)]
14. Teprovich, J.A., Jr.; Colón-Mercado, H.R.; Ward, P.A.; Peters, B.; Giri, S.; Zhou, J.; Greenway, S.; Compton, R.N.; Jena, P.; Zidan, R. Experimental and Theoretical Analysis of Fast Lithium Ionic Conduction in a LiBH_4 - C_{60} Nanocomposite. *J. Phys. Chem. C* **2014**, *118*, 21755–21761. [[CrossRef](#)]
15. Matsuo, M.; Remhof, A.; Martelli, P.; Caputo, R.; Ernst, M.; Miura, Y.; Sato, T.; Oguchi, H.; Maekawa, H.; Takamura, H.; et al. Complex Hydrides with $(\text{BH}_4)^-$ and $(\text{NH}_2)^-$ Anions as New Lithium Fast-Ion Conductors. *J. Am. Chem. Soc.* **2009**, *131*, 16389–16391. [[CrossRef](#)] [[PubMed](#)]
16. GharibDoust, S.P.; Brighi, M.; Sadikin, Y.; Ravnsbæk, D.B.; Černý, R.; Skibsted, J.; Jensen, T.R. Synthesis, Structure, and Li-Ion Conductivity of $\text{LiLa}(\text{BH}_4)_3\text{X}$, X = Cl, Br, I. *J. Phys. Chem. C* **2017**, *121*, 19010–19021. [[CrossRef](#)]
17. Skripov, A.V.; Soloninin, A.V.; Ley, M.B.; Jensen, T.R.; Filinchuk, Y. Nuclear Magnetic Resonance Studies of BH_4 Reorientations and Li Diffusion in $\text{LiLa}(\text{BH}_4)_3\text{Cl}$. *J. Phys. Chem. C* **2013**, *117*, 14965–14972. [[CrossRef](#)]
18. Roedern, E.; Lee, Y.; Ley, M.B.; Park, K.; Cho, Y.W.; Skibsted, J.; Jensen, T.R. Solid state synthesis, structural characterization and ionic conductivity of bimetallic alkali-metal yttrium borohydrides $\text{MY}(\text{BH}_4)_4$ (M = Li and Na). *J. Mater. Chem. A* **2016**, *4*, 8793–8802. [[CrossRef](#)]
19. Ley, M.B.; Ravnsbæk, D.B.; Filinchuk, Y.; Lee, Y.; Janot, R.; Cho, Y.W.; Skibsted, J.; Jensen, T.R. $\text{LiCe}(\text{BH}_4)_3\text{Cl}$, a New Lithium-Ion Conductor and Hydrogen Storage Material with Isolated Tetranuclear Anionic Clusters. *Chem. Mater.* **2012**, *24*, 1654–1663. [[CrossRef](#)]
20. Lee, Y.; Ley, M.B.; Jensen, T.R.; Cho, Y.W. Lithium Ion Disorder and Conduction Mechanism in $\text{LiCe}(\text{BH}_4)_3\text{Cl}$. *J. Phys. Chem. C* **2016**, *120*, 19035–19042. [[CrossRef](#)]

21. Yamauchi, A.; Sakuda, A.; Hayashi, A.; Tatsumisago, M. Preparation and ionic conductivities of $(100 - x)$ $(0.75\text{Li}_2\text{S}-0.25\text{P}_2\text{S}_5)\cdot x\text{LiBH}_4$ glass electrolytes. *J. Power Sources* **2013**, *244*, 707–710. [[CrossRef](#)]
22. Lee, H.; Hwang, S.; To, M.; Lee, Y.; Cho, Y.W. Discovery of Fluidic LiBH_4 on Scaffold Surfaces and Its Application for Fast Co-confinement of LiBH_4 – $\text{Ca}(\text{BH}_4)_2$ into Mesopores. *J. Phys. Chem. C* **2015**, *119*, 9025–9035. [[CrossRef](#)]
23. Takahashi, K.; Hattori, K.; Yamazaki, T.; Takada, K.; Matsuo, M.; Orimo, S.; Maekawa, H.; Takamura, H. All-Solid-State Lithium Battery with LiBH_4 Solid Electrolyte. *J. Power Sources* **2013**, *226*, 61–64. [[CrossRef](#)]
24. Suzuki, S.; Kawaji, J.; Yoshida, K.; Unemoto, A.; Orimo, S. Development of complex hydride-based allsolid-state lithium ion battery applying low melting point electrolyte. *J. Power Sources* **2017**, *359*, 97–103. [[CrossRef](#)]
25. Unemoto, A.; Chen, C.L.; Wang, Z.; Matsuo, M.; Ikeshoji, T.; Orimo, S. Pseudo-binary electrolyte, LiBH_4 – LiCl , for bulk-type all-solid-state lithium-sulfur battery. *Nanotechnology* **2015**, *26*, 254001. [[CrossRef](#)] [[PubMed](#)]
26. Lopez-Aranguren, P.; Berti, N.; Dao, A.H.; Zhang, J.; Cuevas, F.; Latroche, M.; Jordy, C. An all-solid state metal hydride–Sulfur lithium-ion battery. *J. Power Sources* **2017**, *357*, 56–60. [[CrossRef](#)]
27. Unemoto, A.; Ikeshoji, T.; Yasaku, S.; Matsuo, M.; Stavila, V.; Udovic, T.J.; Orimo, S. Stable Interface Formation between TiS_2 and LiBH_4 in Bulk-Type All-Solid-State Lithium Batteries. *Chem. Mater.* **2015**, *27*, 5407–5416. [[CrossRef](#)]
28. Unemoto, A.; Wu, H.; Udovic, T.J.; Matsuo, M.; Ikeshoji, T.; Orimo, S. Fast lithium-ionic conduction in a new complex hydride–sulfide crystalline phase. *Chem. Commun.* **2016**, *52*, 564–566. [[CrossRef](#)] [[PubMed](#)]
29. Hamon, Y.; Brousse, T.; Jousse, F.; Topart, P.; Buvat, P.; Schleich, D.M. Aluminum negative electrode in lithium ion batteries. *J. Power Sources* **2001**, *97–98*, 185–187. [[CrossRef](#)]
30. Buiel, E.; Dahn, J.R. Li-insertion in hard carbon anode materials for Li-ion batteries. *Electrochim. Acta* **1999**, *45*, 121–130. [[CrossRef](#)]
31. Hudak, N.; Huber, D. Size Effects in the Electrochemical Alloying and Cycling-of Electrodeposited Aluminum with Lithium. *J. Electrochem. Soc.* **2012**, *159*, A688–A695. [[CrossRef](#)]
32. Shenouda, A.Y.; Murali, K.R. Electrochemical properties of doped lithium titanate compounds and their performance in lithium rechargeable batteries. *J. Power Sources* **2008**, *176*, 332–339. [[CrossRef](#)]
33. Au, M.; McWhorter, S.; Ajo, H.; Adams, T.; Zhao, Y.; Gibbs, J. Free standing aluminum nanostructures as anodes for Li-ion rechargeable batteries. *J. Power Sources* **2010**, *195*, 3333–3337. [[CrossRef](#)]
34. Oltean, G.; Tai, C.; Edstrom, K.; Nyholm, L. On the origin of the capacity fading for aluminum negative electrodes in Li-ion batteries. *J. Power Sources* **2014**, *269*, 266–273. [[CrossRef](#)]
35. Lei, X.; Wang, C.; Yi, Z.; Liang, Y.; Sun, J. Effects of particle size on the electrochemical properties of aluminum powders as anode materials for lithium ion batteries. *J. Alloys Compd.* **2007**, *429*, 311–315. [[CrossRef](#)]
36. Teprovich, J.A., Jr.; Motyka, T.; Zidan, R. Hydrogen System Using Novel Additives to Catalyze Hydrogen Release from the Hydrolysis of Alane and Activated Aluminum. *Int. J. Hydrog. Energy* **2012**, *37*, 1594–1603. [[CrossRef](#)]
37. Martínez-Rodríguez, M.J.; García-Díaz, B.L.; Teprovich, J.A., Jr.; Knight, D.A.; Zidan, R. Advances in the Electrochemical Regeneration of Aluminum Hydride. *Appl. Phys. A* **2012**, *106*, 545–550. [[CrossRef](#)]
38. Sveinbjörnsson, D.; Myrdal, J.S.G.; Blanchard, D.; Bentzen, J.J.; Hirata, T.; Mogensen, M.B.; Norby, P.; Orimo, S.; Vegge, T. Effect of Heat Treatment on the Lithium Ion Conduction of the LiBH_4 – LiI Solid Solution. *J. Phys. Chem. C* **2013**, *117*, 3249–3257. [[CrossRef](#)]
39. Teprovich, J.A., Jr.; Colon-Mercado, H.; Washington, A.L., II; Ward, P.A.; Hartman, H.; Greenway, S.; Missimer, D.M.; Velten, J.; Christian, J.H.; Zidan, R. Bi-functional $\text{Li}_2\text{B}_{12}\text{H}_{12}$ for energy storage and conversion applications: Solid-state electrolyte and luminescent down-conversion dye. *J. Mater. Chem. A* **2015**, *3*, 22853–22859. [[CrossRef](#)]
40. Teprovich, J.A., Jr.; Zhang, J.; Colón-Mercado, H.; Cuevas, F.; Peters, B.; Greenway, S.; Zidan, R.; Latroche, M. Li-Driven Electrochemical Conversion Reaction of AlH_3 , LiAlH_4 , and NaAlH_4 . *J. Phys. Chem. C* **2015**, *119*, 4666–4674. [[CrossRef](#)]
41. Liu, D.X.; Co, A.C. Revealing Chemical Processes Involved in Electrochemical (De)Lithiation of Al with in Situ Neutron Depth Profiling and X-ray Diffraction. *J. Am. Chem. Soc.* **2016**, *138*, 231–238. [[CrossRef](#)] [[PubMed](#)]
42. Besenhard, J.O.; Hess, M.; Komenda, P. Dimensionally stable Li-alloy electrodes for secondary batteries. *Solid State Ion.* **1990**, *40–41*, 525–529. [[CrossRef](#)]

43. Winter, M.; Besenhard, J.O. Electrochemical lithiation of tin and tin-based intermetallics and composites. *Electrochim. Acta* **1999**, *45*, 31–50. [[CrossRef](#)]
44. Reynier, Y.; Yazami, R.; Fultz, B. XRD evidence of macroscopic composition inhomogeneities in the graphite–lithium electrode. *J. Power Sources* **2007**, *165*, 616–619. [[CrossRef](#)]
45. Gomes, S.; Hagemann, H.; Yvon, K. Lithium boro-hydride LiBH₄: II. Raman spectroscopy. *J. Alloys Compd.* **2002**, *346*, 206–210. [[CrossRef](#)]
46. Li, S.; Niu, J.; Zhao, Y.C.; So, K.P.; Wang, C.; Wang, C.A.; Li, J. High-rate aluminum yolk-shell nanoparticle anode for Li-ion battery with long cycle life and ultrahigh capacity. *Nat. Commun.* **2015**, *6*, 7872. [[CrossRef](#)] [[PubMed](#)]



© 2017 by the authors. Licensee MDPI, Basel, Switzerland. This article is an open access article distributed under the terms and conditions of the Creative Commons Attribution (CC BY) license (<http://creativecommons.org/licenses/by/4.0/>).